Inverse Estimation of Mars 2020 Entry Aeroheating Environments Using MEDLI2 Flight Data

Hannah S. Alpert* and David A. Saunders†
AMA Inc. at NASA Ames Research Center, Moffett Field, CA 94035

Milad Mahzari‡, Joshua D. Monk§, and Todd R. White¶
NASA Ames Research Center, Moffett Field, CA 94035

The Mars Entry, Descent, and Landing Instrumentation 2 (MEDLI2) sensor suite collected heating and pressure data during entry into Mars' atmosphere of the Mars 2020 Perseverance rover. MEDLI2 included thermocouples, heat flux sensors, and pressure transducers on both the heatshield and the backshell. This paper covers the inverse estimation of heatshield and backshell surface heating based on the MEDLI2 Instrumented Sensor Plugs (MISPs), a network of thermocouples embedded in thermal protection system plugs across the aeroshell. Monte Carlo analysis was conducted to assess the sensitivity of the surface heat rate and temperature to uncertainties in thermocouple depth and material properties such as density, specific heat capacity, and thermal conductivity. Data from each MISP was also used to estimate the local time of transition from laminar to turbulent flow at each plug location.

I. Nomenclature

C_H	=	Heat transfer coefficient
C_p	=	Specific heat capacity
d	=	Depth
k	=	Thermal conductivity
q	=	Heat rate
r	=	Radius
T	=	Temperature
$\mathbf{T}$	=	Vector of direct problem outputs (FIAT predictions)
x_i	=	Discrete control points
$\mathbf{Y}$	=	Vector of measurements
α	=	Surface absorptivity
ϵ	=	Surface emissivity
λ	=	Regularization parameter
μ	=	Mean
σ	=	Standard deviation
σ_{SB}	=	Stefan-Boltzmann constant

Subscripts

c	=	Char
$cond$	=	Conduction
s	=	Surface
v	=	Virgin
w	=	Wall
∞	=	Freestream

*Systems Engineer, Entry Systems and Vehicle Engineering Branch.
†Senior Research Scientist, Aerothermodynamics Branch, AIAA Senior Member.
‡Aerospace Engineer, Entry Systems and Vehicle Engineering Branch, AIAA Member.
§Aerospace Engineer, Thermal Protection Materials Branch.
¶Senior Research Scientist, Entry Systems and Vehicle Engineering Branch, AIAA Senior Member.

II. Introduction

The Mars Entry, Descent, and Landing Instrumentation 2 (MEDLI2) sensor suite collected data during the entry of the Mars 2020 Perseverance rover into Mars' atmosphere on February 18, 2021. MEDLI2 included thermocouples (TCs), heat flux sensors, and pressure transducers to measure the extreme heating and pressure on both the heatshield and the backshell throughout this period [1]. While only the heatshield portion of the aeroshell was instrumented on Mars Science Laboratory (MSL) [2], the addition of backshell instrumentation in MEDLI2 provides NASA's first direct measurements of aerothermal heating on an entry vehicle's backshell at Mars [3]. These flight data can be compared with pre-flight aerothermal predictions to update analytical models and improve the designs of entry systems for future missions.

The Mars 2020 entry vehicle aeroshell was nearly identical to the MSL aeroshell. Its thermal protection system (TPS) was comprised of a 4.5-meter diameter, 70° sphere-cone heatshield made of Phenolic Impregnated Carbon Ablator (PICA) tiles and a biconic backshell made of Super Lightweight Ablator (SLA-561V). The parachute closeout cone and the backshell interface plate were protected with Acusil II [4]. PICA, made of a carbon fiber preform impregnated with phenolic resin [5], has been used successfully on previous missions, including Stardust in 1999 [6] and MSL in 2011 [7]. SLA-561V was used on the Viking, Pathfinder, and Mars Exploration Rovers missions, among many others, and is a mixture of ground cork, silica, and phenolic in a silicone binder [8]. Additionally, the heatshield was sprayed with a thin silicone coating called NuSil® to prevent contamination of spacecraft sensors with particles shed by PICA.

This paper focuses on the inverse estimation of the Mars 2020 entry vehicle's surface heating based on the MEDLI2 Instrumented Sensor Plugs (MISPs), a network of thermocouples embedded in TPS plugs that were flush-mounted throughout the heatshield and backshell. It builds off the work done to reconstruct the aeroheating of the MSL heatshield using the data from the MEDLI suite [9–12], using many of the same principles, but also utilizing the additional thermocouple plugs in the backshell.

Section III describes the MISP instrumentation and flight data in more detail. Section IV describes the inverse reconstruction methodology used to determine surface heating as well as the material property uncertainties used in the Monte Carlo simulations to determine the confidence bounds on the reconstructed heating. Section V provides the final reconstructed surface heat flux and temperature, along with their associated 95% confidence intervals. The time at which the flow transitioned from laminar to turbulent is also estimated at each plug location and presented in this section. While this paper focuses on the inverse analysis of the flight data, references [13–17] discuss the comparisons between the reconstructed heat flux and the direct measurements taken with heat flux gauges and radiometers, comparisons between the reconstructed environments and the environments predicted by CFD, and the specifics of the material models used for this analysis.

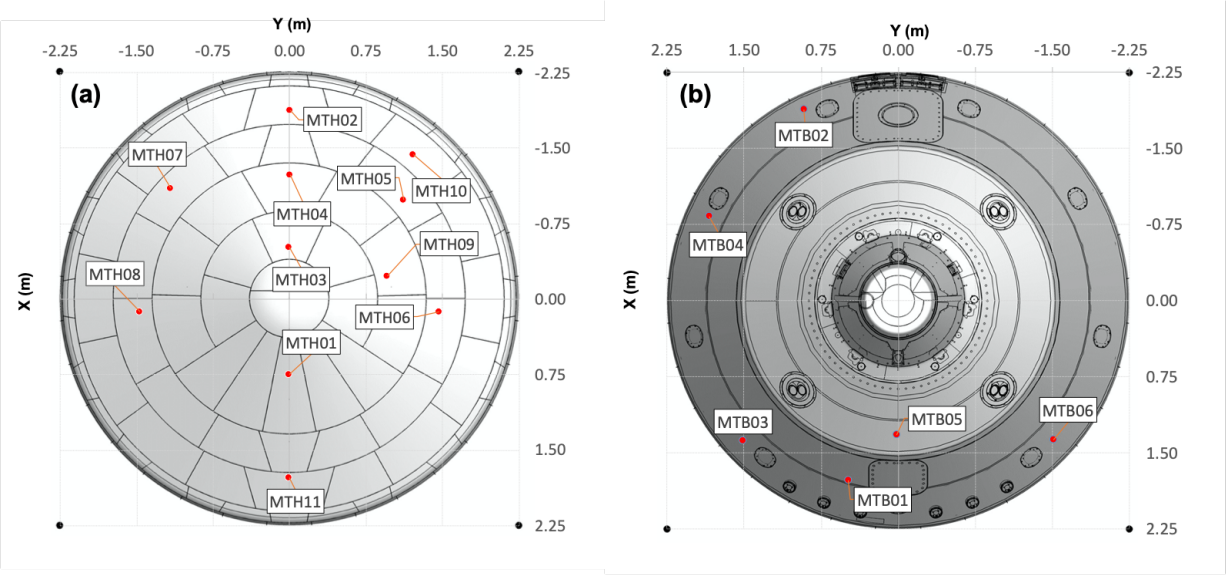

Fig. 1 Locations of MISPs on (a) heatshield and (b) backshell, where the wind side is at the bottom.

III. MISP Instrumentation

MEDLI2 consists of three major subsystems: Mars Entry Atmospheric Data System (MEADS), MISPs, and Sensor Support Electronics (SSE). MEADS is comprised of a network of 8 hypersonic, supersonic, and low-pressure transducers on the heatshield and the backshell. MISP consists of a network of high-temperature thermocouples embedded within TPS plugs across the heatshield and the backshell, as well as 2 total heat flux sensors on the backshell to measure total surface heat flux and 1 radiometer on the backshell to measure radiative-only heating. Finally, the SSE includes the avionics needed to gather, process, and transfer the MISP and MEADS data [18]. As shown in Fig. 1, 11 MISPs denoted MTH01-MTH11 (MISP Thermal on Heatshield) were placed across the heatshield to capture turbulent flowfield transition, while 6 MISPs denoted MTB01-MTB06 (MISP Thermal on Backshell) were placed on the backshell to capture the aeroheating in regions of attached and detached flow. The heatshield MISPs were made of PICA and the backshell MISPs were made of SLA-561V, matching the aeroshell TPS materials they were embedded in. Each heatshield MISP is a cylinder with a diameter of 33 mm and a height of 29 mm, with 1 or 3 thermocouples embedded within the cylinder. The backshell MISPs have a diameter of 31.5 mm and a depth of 10 mm, and have 1 or 2 thermocouples embedded. A diagram and a photograph of a heatshield MISP and a backshell MISP are shown in Fig. 2 and Fig. 3, respectively. The near-surface TC in each heatshield MISP is R-type, while the deeper TCs in the heatshield MISP and all of the TCs in the backshell MISPs are K-type [18]. Only the near-surface TC in each MISP was used for heating reconstruction; the deeper TCs were intended for use in the assessment of the material's in-depth thermal response. The near-surface thermocouples are at nominal design depths of 0.075 in. (1.91 mm) beneath the surface for MTH01-03 and 0.1 in. (2.54 mm) beneath the surface for the rest (MTH04-11 and MTB01-06). The actual X-ray measured depths of each thermocouple are shown in Table 1 and Table 2 for the backshell and heatshield, respectively. The TC measurements used for reconstruction were sampled at 8 Hz. In this paper, time 0 denotes the entry interface time. The entry interface was defined at a radius of 3522.2 km based on the best estimated trajectory and corresponds to a spacecraft clock time of 666,952,519.626878 s [19].

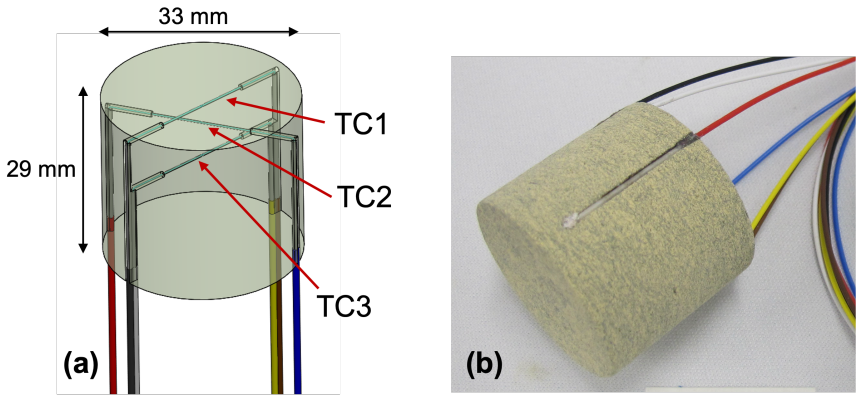

Fig. 2 (a) Diagram and (b) image of a heatshield MISP with three thermocouples.

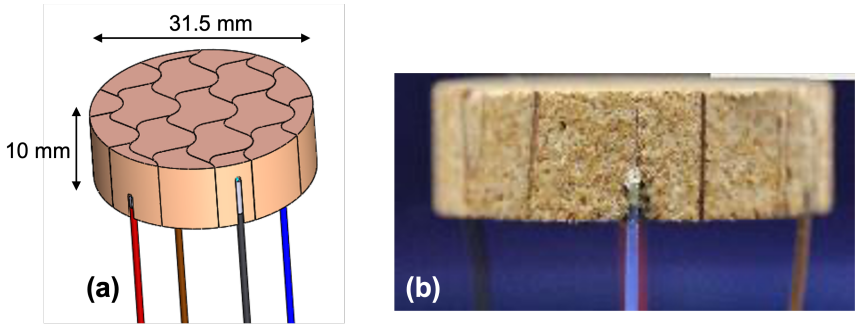

Fig. 3 (a) Diagram and (b) image of a backshell MISP with two thermocouples.

Table 1 Design and X-ray measured depths of MISP thermocouples in backshell (all measurements in inches).

	Design	MTB01	MTB02	MTB03	MTB04	MTB05	MTB06
TC1	0.10	0.1009	0.1027	0.1028	0.1031	0.1030	0.1028
TC2	0.25	0.2506	-	-	-	-	-

Table 2 Design and X-ray measured depths of MISP thermocouples in heatshield (all measurements in inches).

	Design	MTH01	MTH02	MTH03	MTH04	MTH05	MTH06	MTH07	MTH08	MTH09	MTH10	MTH11
TC1	0.075 to 0.10	0.0781	0.0769	0.0756	0.1013	0.1018	0.1016	0.1014	0.1017	0.1018	0.1019	0.1015
TC2	0.2	0.2014	0.2006	0.2033	-	-	-	-	-	-	-	-
TC3	0.45	0.4500	0.4533	0.4537	-	-	-	-	-	-	-	-

IV. Inverse Reconstruction Methodology

The heating reconstruction was done with a NASA-developed program called *FIAT_Opt*, which utilized the Fully Implicit Ablation and Thermal Response (FIAT) tool also developed at NASA [20] – in this case, FIAT v3.2.0 was used. FIAT simulates one-dimensional heat conduction, material decomposition, pyrolysis gas generation, and surface ablation using equilibrium chemistry models. Generally, the aerothermal environment and material stack-up are input into FIAT, and the output is the thermal response of the material throughout its depth; however, for this analysis, the opposite was desired. Because the thermocouples are embedded within the TPS material, the reconstruction of surface heating is posed as an inverse problem in which the surface heating is estimated by minimizing an objective function of the difference between the FIAT predictions and the MISP temperature data. The *FIAT_Opt* program adjusts the the surface heating profile (discrete control points along the heating profile, denoted as x_i in this paper) until there is a close match between the flight TC data and the FIAT temperature predictions at the corresponding TC depth. While there were between one and three thermocouples embedded within each plug, the flight temperatures from the shallowest thermocouple were used in this analysis due to its having the highest sensitivity to surface heating and the least sensitivity to material property uncertainty. The flight data from the shallowest thermocouple are shown in Fig. 4. Even the shallowest thermocouples, just 1.91 mm below the surface, survived the flight, suggesting that very little material recession occurred. Further, the heatshield was coated by NuSil® which is known to inhibit oxidation, the primary mechanism for PICA recession [21]; ground testing of coated PICA samples has shown that NuSil® survives at heating conditions relevant to Mars2020 [22]. Therefore, the surface heating was estimated assuming no material recession, and the following surface energy balance option in FIAT was specified:

$$q_s + \alpha_w q_{rad} - \sigma_{SB}\epsilon_w(T_w^4 - T_\infty^4) - q_{cond} = 0 \tag{1}$$

Convective heating (q_s) and radiative heating (q_{rad}) cannot be simultaneously estimated since they have a very similar effect on in-depth temperatures. Therefore, reconstructed in this paper is the $q_s + \alpha_w q_{rad}$ term, which includes both absorbed radiative heat flux and convective heating (including transpiration cooling effects from the pyrolysis gases).

A. Material Stack-up

The PICA and SLA-561V models used in this analysis were based on those used for MSL, but fine-tuned according to the flight lot testing conducted by the MEDLI2 project [15]. The NuSil® layer on the heatshield is not included because its thickness has not been well characterized and its material response model had not been validated at the time of this analysis. The material stack-ups used were based on the structure of the flight vehicle at each MISP location.

B. Gauss-Newton Method

The Gauss-Newton-class method used for this analysis is a whole-time domain method in which the entire heating profile is estimated using the full in-depth temperature measurement time history. The alternative to this would be a sequential method, in which the surface heating is estimated using a small subset of the measurements and proceeds sequentially in time. The Gauss-Newton method is applicable to nonlinear least-squares problems, and while it does not require the knowledge of second derivatives (because it approximates them), it does require the computation of the first-derivative Jacobian matrix: $\frac{\partial f_i}{\partial x_i}$ for $F(x) = \Sigma f_i(x)^2$. This computation (by finite differencing) can require hundreds

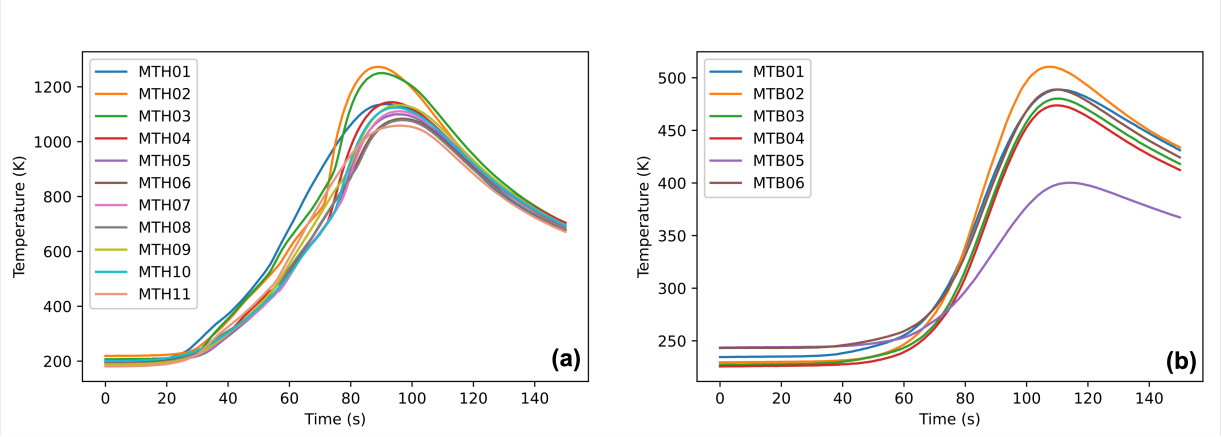

Fig. 4 Temperature data from shallowest thermocouple from (a) heatshield MISPs and (b) backshell MISPs.

of FIAT simulations at each minimization iteration because each evaluate of $F(x)$ needs a FIAT result. Two to three FIAT calls per CPU second, 20-40 iterations, and 150+ function evaluations per iteration with 150 variables represent the typical performance on a single processor, leading to a total run time of ~30 minutes.

The objective function that is minimized through this method is $F(x) = \Sigma(Y_i - T_i)^2$ where $\mathbf{Y}$ is the vector of flight temperature measurements and $\mathbf{T}$ is the corresponding vector of temperature predictions by FIAT. Tikhonov regularization [23] used in tandem with the Gauss-Newton method has been found to produce the best results among the family of related choices (another being the Levenberg-Marquardt algorithm [24, 25]). The Tikhonov technique involves augmenting the objective with a penalty function $\lambda^2\Sigma(x_{i+1} - x_i)^2$ to inhibit oscillations (that are likely otherwise because the problem is ill-posed) and instabilities in the solution due to noisy data (although the MEDLI2 data prove to be remarkably clean). In the penalty function, λ is called the regularization parameter, and dictates the degree of smoothing in the solution. These methods are described in further detail in Ref. [9].

FIAT_Opt employs a step-halving line search at each step, meaning that if the objective function increases instead of decreasing at the start of each step, the step length is reduced (typically by a factor of 0.5). The step is reduced repeatedly if necessary until the objective has been reduced by the specified percentage (say 0.01%) or until the step length has reached a lower limit. If the objective cannot be reduced sufficiently, the iteration terminates and has normally bottomed out with a close fit to the target in-depth temperature data. There is no gradient-based convergence test, and an iteration limit of 40 is seldom encountered with 150 control points.

C. FIAT_Opt Inputs

FIAT_Opt requires six input files, as described below:

1) A file that includes the material stack-up at the location of interest on the heatshield or backshell as well as the initial temperatures and the TC depths. In this analysis, the stack-ups used were based on the structure of the flight vehicle at each MISP location.
2) A materials database file containing the temperature- and pressure-dependent material properties of each material, both virgin and char, in the stack-up, including porosity, density, specific heat capacity, emissivity, and thermal conductivity, among others.
3) A file that contains surface environmental distributions for total heat flux, radiative heat flux, heat transfer coefficient, pressure, and fluid temperature, throughout the timeframe of interest. In this analysis, these initial guesses were the predicted flight environments derived from CFD results. Only one of these surface distributions, either C_H or total heat flux, is estimated by the optimization, while the other quantities are presumed known and fixed; in this paper, total heat flux was estimated via inverse analysis.
4) A file that contains an initial guess of the parameter to be estimated (heat transfer coefficient or combined heat flux) over the timeframe of interest with as many control points vs. time as intended for the initial optimization. These are splined at the indicated uniform resolution along with the surface distributions of the other quantities, which do not change after the initial interpolations. For the analyses shown, 150 variables at 1 s intervals were used in two-optimization runs. Performing more than one optimization in the same run allows a solution to

be refined by switching from forward to central differencing (twice as expensive, but more accurate) for the Jacobian matrix calculations, and by inserting an extra control point at the current heat pulse peak and another at the estimated transition time, and also by applying sinusoidal weighting centered on the location of the largest current temperature deviation. The 150 becomes 152 control points if these options are turned on.

5) A file containing the flight temperature data for the timeframe of interest, interpolated in the cases shown to a uniform 4 Hz frequency over 150 s. These are the target temperatures to be fitted as well as possible with FIAT-predicted temperatures by optimizing the surface heat pulse variables.
6) A file specifying the optimization parameters to be used, further described in the next section (Section IV.D).

D. Optimization Parameters

FIAT_Opt has many control variables entered via a namelist that specify the optimization parameters. All of them are defaulted, and the more significant controls are described here.

- **Number of optimizations**: The Monte Carlo runs documented here were all performed with two optimizations of 150 (+2) variables and the next-optimization refinements described in #4 above (i.e., switching from forward to central differencing, inserting extra control points at heat pulse peak and transition location, and applying sinusoidal weighting).
- **Interpolation of control points**: Monotonic local spline interpolation of the control points at uniform intervals of 0.5 s was used, as it copes well with oscillations that commonly appear temporarily during an optimization.
- **Regularization parameter**: A value of 2 was found to be appropriate for the regularization parameter λ to inhibit the oscillatory solutions that are often present with no regularization. The term λ^2 is applied to the sum of squared differences between adjacent heat pulse variables.
- **Variable scaling**: Variables are scaled to the first order to improve optimizer stability/convergence. Scaling also allows for using the same regularization parameter for all MISP locations. In this analysis, a scaling factor of 10 was used, meaning the physical variables are 10 times the optimization variables.
- **Trust radius**: The trust radius strongly affects convergence behavior, as it limits the fractional change of each variable by the given amount (e.g., a trust radius of 0.3, as used here, limits the fractional change of each variable to no more than 30% at each iteration).

E. Monte Carlo

A Monte Carlo analysis was performed on the inverse estimation procedure to evaluate the uncertainty associated with the estimated surface heating profiles at all MISPs. The material model and sensor parameters used in the Monte Carlo analysis include density (ρ), specific heat capacity (C_p), emissivity (ϵ), thermal conductivity (k) and TC depth (d). Uncertainties were determined based upon the MEDLI2 flight-lot testing; an example for the thermal conductivity of virgin and char PICA is shown in Fig. 5. The uncertainties associated with each material/sensor parameter are listed in Tables 3 and 4, where subscripts v and c are used to denote virgin and char properties respectively. The virgin and char density for both PICA and SLA-516V were assumed to have a uniform distribution (U), while the rest of the aforementioned parameters were assumed to have normal distributions (N). Additionally, the depth of the thermocouples within the TPS plug were determined to have an uncertainty of 0.003 in., also assumed to be distributed normally around the X-ray measured TC depth.

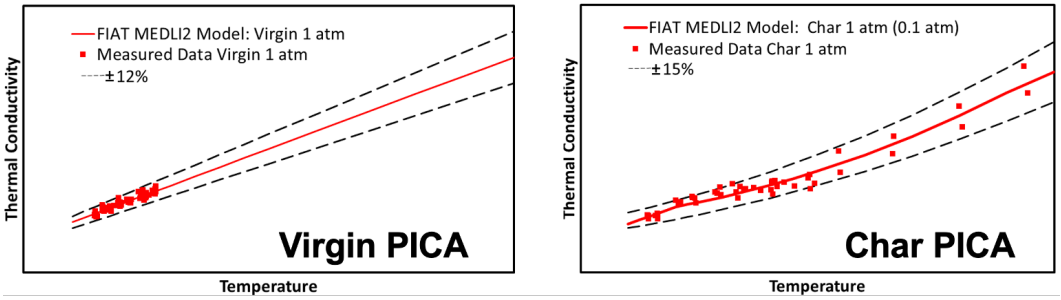

Fig. 5 Thermal conductivity of flight-lot virgin and char PICA with associated uncertainty bounds included (dashed lines).

Table 3 Uncertainties associated with backshell MISPs (SLA-516V).

	$\rho_v = \rho_c$	$C_{p,v} = C_{p,c}$	ϵ_v	ϵ_c	$k_v = k_c$	d
Distribution	U	N	N	N	N	N
$2\sigma/\mu$	±0.018*	0.15	0.15	0.15	0.13	0.003" **
*Upper/lower bound for the uniform distribution, **not** $2\sigma/\mu$.						
2σ **not $2\sigma/\mu$.						

Table 4 Uncertainties associated with heatshield MISPs (PICA).

	$\rho_v = \rho_c$	$C_{p,v} = C_{p,c}$	ϵ_v	ϵ_c	k_v	$k_c^\dagger$	d
Distribution	U	N	N	N	N	N	N
$2\sigma/\mu$	±0.018*	0.05	0.03	0.03	0.12	0.15	0.003" **
*Upper/lower bound for the uniform distribution, **not** $2\sigma/\mu$.							
2σ **not $2\sigma/\mu$.							
†Uncertainty scaled by 15/12 (i.e., virgin and char are linked).							

Once the distributions were generated and 2000 samples were taken for the Monte Carlo simulations, the 2000 samples were assessed to ensure that they matched the desired distributions. An example of the sampled distributions for MTB03 is shown in Fig. 6, confirming appropriate Gaussian behavior of the samples.

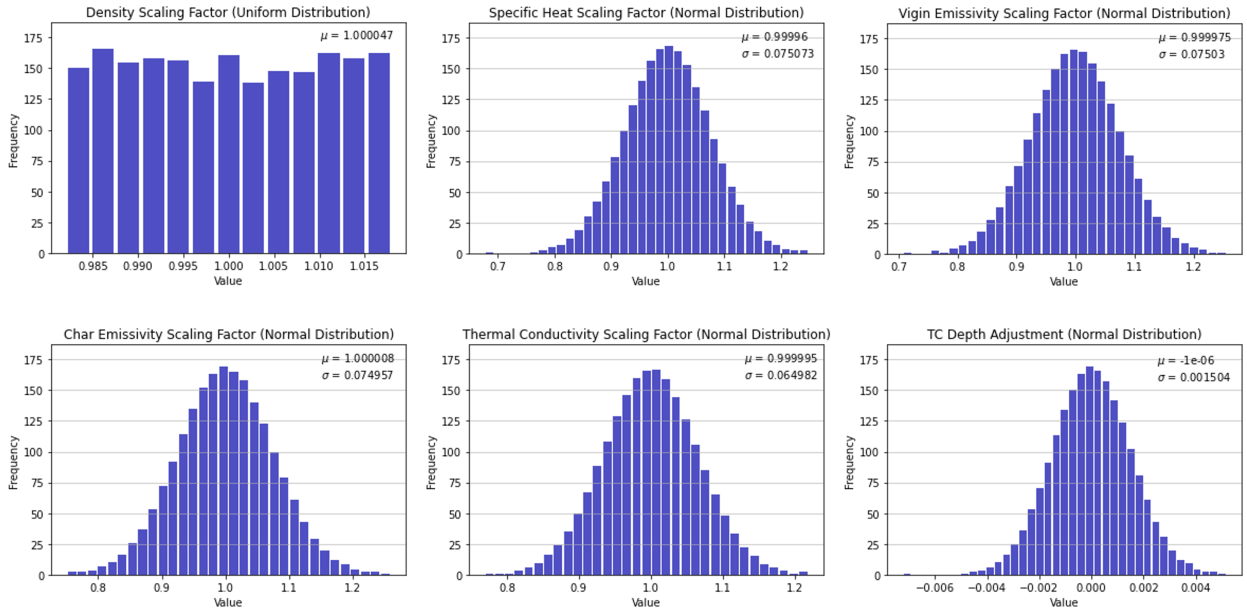

Fig. 6 Sampled distributions for the material and sensor parameters included in the Monte Carlo simulation for MTB03.

After the simulation was run, the standard deviation at the peak heat flux for each Monte Carlo iteration was plotted to verify that a sufficient number of cases were being evaluated. For each of the MISPs, the standard deviation appeared to remain stable after 500-750 iterations, indicating that 2000 iterations were sufficient. Examples are shown for the MISPs with the highest and lowest peak heat fluxes (MTH02 and MTB05, respectively) in Fig. 7.

The 95% confidence intervals were determined in two different ways. In the first method, the standard deviation (σ) at each time point was calculated, and the confidence interval was determined to be $1.96 \times \sigma$. In the second method, the

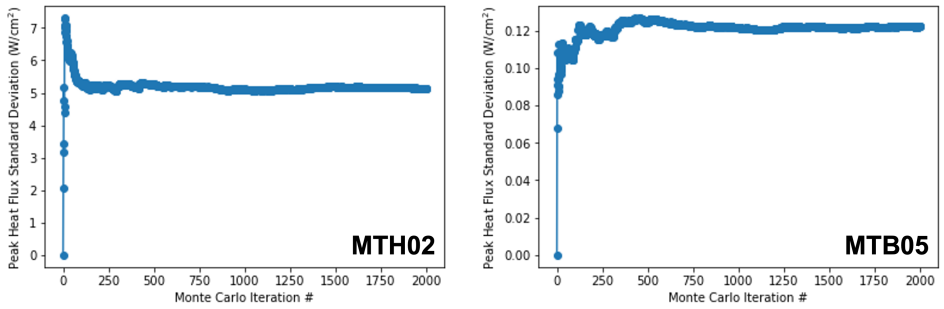

Fig. 7 Standard deviation at the peak heat flux for each Monte Carlo iteration for the MISPs with the highest and lowest peak heat fluxes, MTH02 and MTB05.

highest and lowest 2.5% of heat fluxes (i.e., the 50 highest and the 50 lowest) at each time point were discarded, and the remaining bounds were established as the 95% confidence interval. As shown in Fig. 8, these two methods resulted in very similar bounds, and the second method was selected for use in the ensuing analysis.

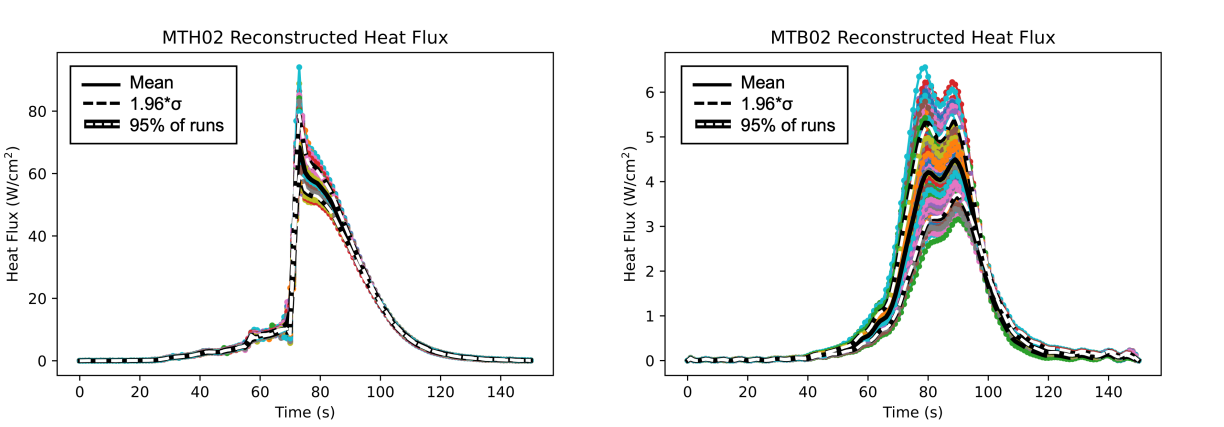

Fig. 8 Reconstructed surface heat fluxes for the MISPs with the highest peak heat fluxes on the backshell (MTB02) and heatshield (MTH02). All 2000 cases are plotted in addition to the mean and the two methods used to determine the 95% confidence interval.

V. Inverse Heating Estimation

The combined surface heat rate throughout entry was reconstructed for each of the backshell and heatshield MISPs and their 95% confidence intervals were determined through Monte Carlo simulations. Using the reconstructed surface heat rate, the estimated surface temperature could also be calculated.

A. Surface Heat Rate Estimation

The reconstructed surface heat flux profiles for the heatshield and backshell are shown in Fig. 9, where each circular point on the plot is a "control point." Peak heating tended to be highest on the leeside for both the heatshield and the backshell, with MTH02 experiencing a peak surface heat rate of 68.4 W/cm^2 and MTB02 reaching a peak of 4.5 W/cm^2. On the heatshield, the heating is higher for the windside plugs (MTH01 and11) in the first 70 seconds and decreases the further we get from the stagnation point (near MTH01). This trend is consistent with pre-flight predictions for laminar flow. However, starting at 70 s, a sharp increase in the heat flux can be observed for the majority of the plugs, starting with the plug farthest away from the stagnation point (MTH02); this sharp increase indicates transition to turbulent flow. The transition front moves inward over the next 11 seconds, eventually encompassing all plugs except MTH01 and MTH11. This trend is consistent with the pre-flight predictions for turbulent flow on a lifting entry vehicle. The

determination of the time of transition from laminar to turbulent flow is described in more detail in Section V.D.

On the backshell, the MISPs with the same radial location (MTB03, MTB04, and MTB06) all had the same heating, except for MTB02; the higher heating on the leeside supports the design concern that backshell heating would be driven by radiative heating, specifically on the leeside. MTB05, which is on the secondary cone, experienced the lowest peak heating, as expected. The reconstruction also shows a double pulse feature at the peak. This may be caused by convective and radiative heat pulses being slightly offset in time from one another, but further analysis is required for confirmation. Other possible explanations include effects from the material response model or TC errors.

Making a direct comparison between pre-flight numerical predictions and reconstructed heat flux profiles presents a challenge because certain assumptions are incorporated into typical CFD-derived environments, which makes it challenging to directly compare them to the reconstructed heating (e.g., no gas-surface reactions, no pyrolysis gas blowing, radiative equilibrium temperature). Despite this, a preliminary comparison between the reconstructed heat fluxes produced in this work and CFD predictions based on the best estimated trajectory (BET), presented in Ref. [17], shows consistent results between the two. Further work is needed to reconcile the differences in surface assumptions between reconstructed and CFD-predicted heat fluxes.

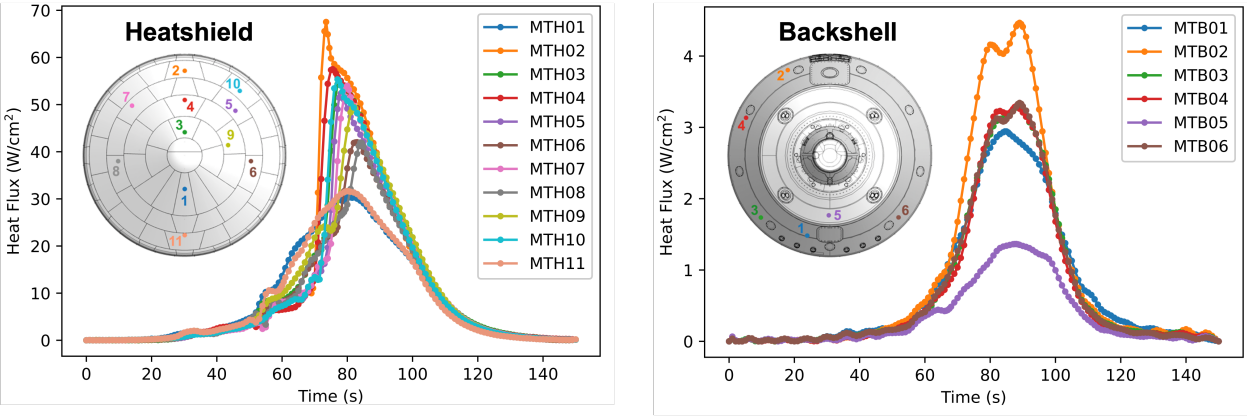

Fig. 9 Reconstructed surface heat fluxes for all (a) heatshield MISPs and (b) backshell MISPs.

B. Surface Temperature Estimation

Because *FIAT_Opt* enables the estimation of the aerothermal environment, the final environment can be used in turn to estimate several surface and in-depth heating parameters over the timeframe, such as surface mass flux, optical and physical material properties, depth of pyrolysis, and temperatures at the surface and throughout the structure. The temperature at the surface is of interest because it provides further insight into the Martian atmosphere and the aeroshell material performance. As such, the reconstructed surface temperatures are shown in Fig. 10.

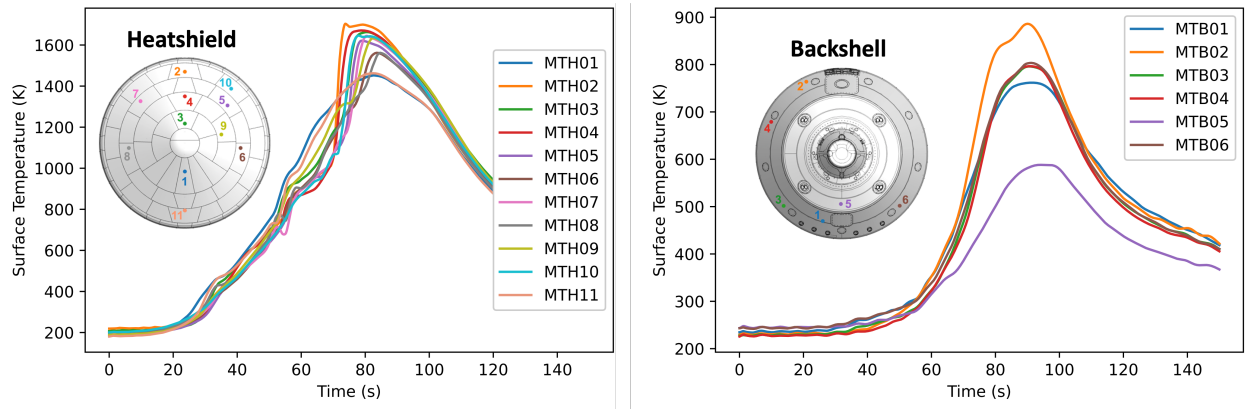

Fig. 10 Reconstructed surface temperatures for all (a) heatshield and (b) backshell MISPs.

C. Monte Carlo Results

The 95% confidence intervals on the nominal heat rates and surface temperatures were calculated based on Monte Carlo simulations in which material properties were varied for each of 2000 cases, based on the uncertainties discussed in Section IV.E. The reconstructed surface heat flux profiles with the associated 95% confidence intervals are shown in Fig. 11 and Fig. 12 for the heatshield and backshell, respectively, and listed in Table 5. The standard deviation derived from the Monte Carlo results for all MISPs is shown in Fig. 13. The MISPs with higher heating were also shown to have higher uncertainty. The maximum standard deviation at peak heat flux is about 5.5 W/cm^2 on the heatshield (MTH02) and 0.6 W/cm^2 on the backshell (MTB02), which is equivalent to 8% and 13% of peak heat flux, respectively. Additionally, Table 6 contains the estimated peak surface temperature with 95% confidence interval for all MISPs. The uncertainty determined by the Monte Carlo runs tended to be dominated by the relatively high uncertainties associated with the specific heat capacity and thermal conductivity.

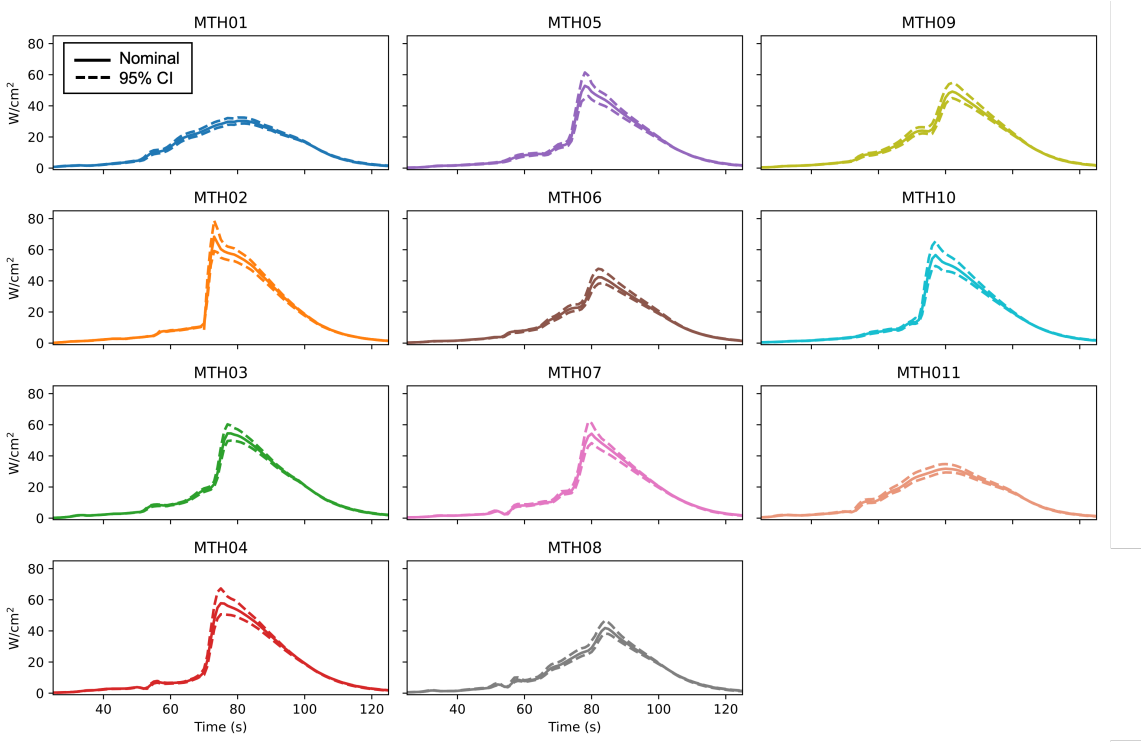

Fig. 11 Reconstructed surface heat fluxes for all heatshield MISPs, with the nominal case and the 95% confidence intervals plotted.

D. Transition from Laminar to Turbulent Flow

The transition from laminar to turbulent flow over the heatshield was observed at all MTH locations except MTH01 and MTH11, which were located on the windside of the heatshield. The transition times were determined in two ways that produced similar results: 1) calculating when there was a distinct change in the slope of the flight temperature data, and 2) assessing when the reconstructed heat flux showed a sudden significant increase, as shown in Fig. 14. The second method is likely more accurate because it is less affected by heat conduction thermal lag, which would delay the calculated transition time.

Transition is more likely to occur further from the stagnation point, as the boundary layer grows in thickness and is thus more susceptible to instabilities, ultimately leading to the transition from laminar to turbulent flow. Thus, transition is observed first at MTH02, and eventually occurs at all MISP locations except for MTH01 and MTH11 locations due to their proximity to the stagnation point. A summary of the estimated transition time with ±1 second accuracy is listed in Table 7, and discussed further in Ref. [13].

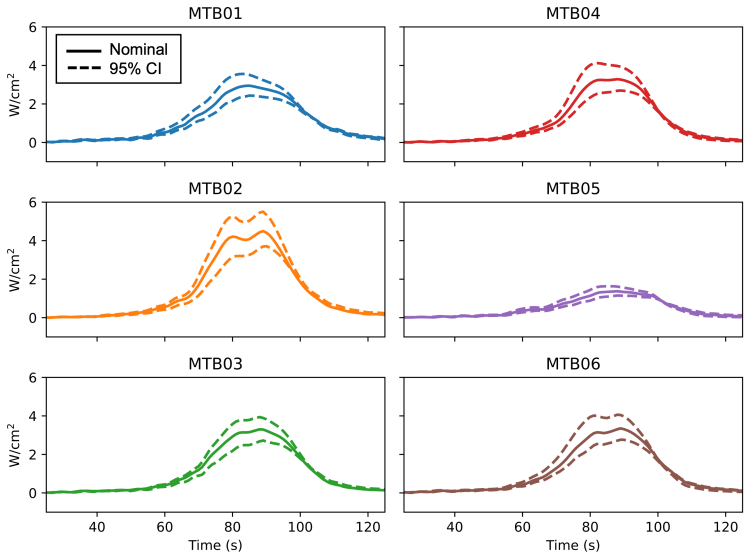

Fig. 12 Reconstructed surface heat fluxes for all backshell MISPs, with the nominal case and the 95% confidence intervals plotted.

Table 5 Estimated peak nominal heat rate with a 95% confidence interval and nominal heat load for all MISPs.

	Combined Heating (W/cm^2)		Heat Load (J/cm^2)	
	Nominal	95% Confidence Interval	Nominal	95% Confidence Interval
Backshell				
MTB01	2.95	2.40-3.52	109.0	93.9-124.9
MTB02	4.50	3.64-5.34	138.3	118.4-166.5
MTB03	3.31	2.68-3.94	108.4	92.9-125.3
MTB04	3.28	2.64-4.03	103.3	89.6-124.0
MTB05	1.38	1.14-1.62	51.7	46.4-58.0
MTB06	3.35	2.71-3.99	108.5	92.8-127.8
Heatshield				
MTH01	30.4	28.6-32.6	1296.5	1236.9-1375.5
MTH02	68.4	59.1-78.8	1672.5	1573.2-1772.6
MTH03	54.5	49.8-60.2	1584.7	1518.0-1656.3
MTH04	57.7	50.6-67.3	1593.1	1491.4-1693.5
MTH05	52.8	46.2-61.5	1398.0	1294.2-1502.1
MTH06	42.4	38.5-47.8	1294.7	1218.8-1398.8
MTH07	54.3	48.2-61.9	1426.4	1329.8-1510.4
MTH08	41.9	38.2-46.8	1276.8	1211.7-1376.4
MTH09	49.2	44.9-54.8	1510.3	1424.7-1638.2
MTH10	56.6	49.6-65.5	1495.7	1405.3-1627.6
MTH11	31.7	29.4-34.7	1276.9	1206.8-1377.5

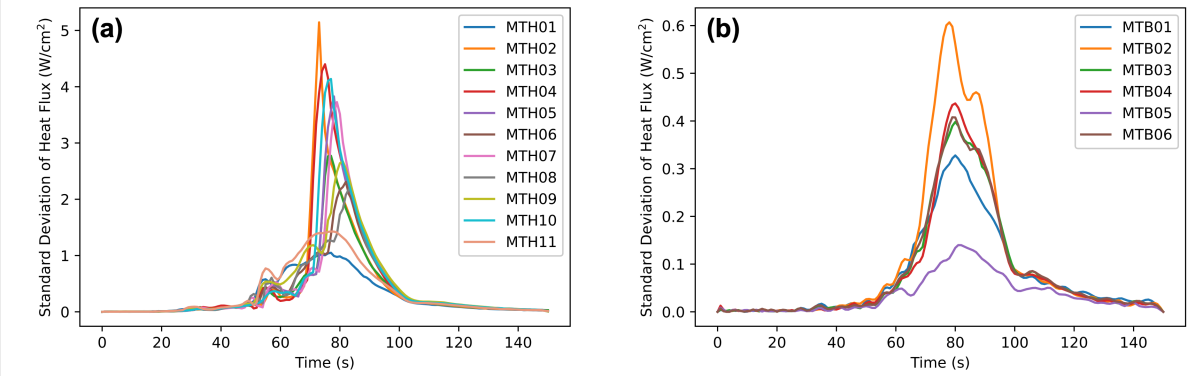

Fig. 13 Standard deviation derived from the Monte Carlo results for all (a) heatshield and (b) backshell MISPs.

Table 6 Estimated peak surface temperature with 95% confidence interval for all MISPs.

	Nominal (K)	95% Confidence Interval (K)
Backshell		
MTB01	762	725-805
MTB02	886	833-943
MTB03	796	751-847
MTB04	797	751-849
MTB05	589	562-620
MTB06	804	758-855
Heatshield		
MTH01	1452	1421-1483
MTH02	1701	1655-1771
MTH03	1663	1620-1711
MTH04	1673	1614-1746
MTH05	1626	1553-1699
MTH06	1562	1509-1617
MTH07	1643	1575-1717
MTH08	1562	1512-1613
MTH09	1632	1578-1686
MTH10	1650	1587-1728
MTH11	1463	1423-1504

Table 7 Estimated time of laminar-to-turbulent transition (s) at locations of heatshield MISPs, listed in order of transition time.

MTH02	MTH04	MTH03	MTH10	MTH05	MTH07	MTH09	MTH06	MTH08	MTH01	MTH11
70	71	73	73	74	75	77	78	81	x	x

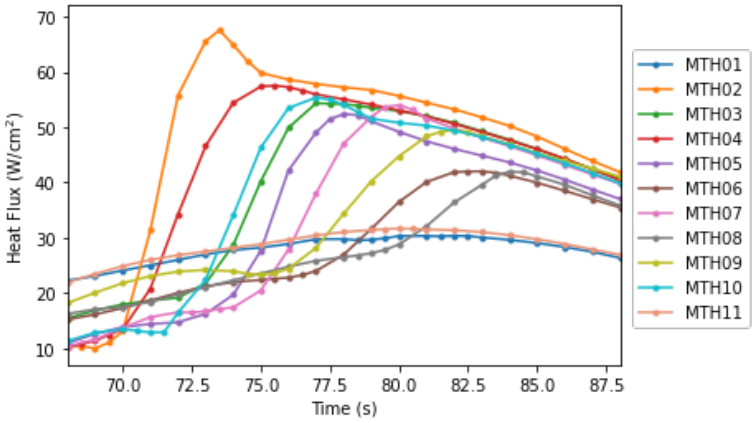

Fig. 14 Reconstructed heat flux of heatshield MISPs, where the transition time from laminar to turbulent flow was calculated for each MISP based on when it experienced a sharp increase in heating.

VI. Conclusion

The Mars 2020 thermocouple flight data were used to reconstruct the aeroheating environment during entry into the Martian atmosphere. The network of MISPs throughout the heatshield and backshell enabled the inverse estimation of heat flux and surface temperature at different locations across the aeroshell, as well as the time of transition from laminar to turbulent flow on the heatshield. A Monte Carlo analysis was performed in order to assess the uncertainty in the reconstructed environments due to uncertainties in the material properties and TC depths, resulting in peak standard deviations of 8% and 13% of peak heat flux for the heatshield and backshell, respectively.

Future work includes reconciling the differences in surface assumptions between reconstructed and CFD-predicted heat fluxes. Currently, the CFD solutions ignore gas-surface reactions and pyrolysis gas blowing, and also assume radiative equilibrium temperature. Despite these challenges, the magnitude of the reconstructed heat flux profiles across the heatshield and backshell were in family with pre-flight numerical predictions [17], meaning there may be an opportunity to reduce design margins in the future.

Another area of future work is the inclusion of NuSil® into the aeroheating reconstruction analysis. After manufacturing the PICA heatshield, a very thin (nominally 220 μm) layer of NuSil® was sprayed onto it to protect the spacecraft sensors from contamination by the particulate matter that is shed by PICA. Its primary effect is inhibiting recession. This was accounted for in the assumption of no material recession, but the presence of NuSil® was otherwise ignored in this analysis due to the lack of a fully-validated NuSil® model. Including NuSil® will likely increase the estimated heat fluxes presented in this paper due to 1) the thermal mass of NuSil® and 2) the fact that the TC depth will be increased by the thickness of NuSil® laying above the plug surface, thus requiring a higher heat flux for the in-depth TC to reach the same temperature. Quantifying the impact of NuSil® on the reconstructed heat fluxes will be pursued over the next 2-3 years under an effort called "MEDLI2 Deep Dive" funded by NASA's Entry Systems Modeling (ESM) project. This will include the development of a high-fidelity thermal response model for NuSil®, its validation against ground testing data, and better characterization of the NuSil® thickness on the MEDLI2 heatshield. The uncertainties associated with NuSil® will be incorporated into the Monte Carlo analysis to further evaluate the impact it may have on the reconstructed aerothermal environments. Future missions could consider having MISPs both with and without NuSil® to provide a comparison during entry environment reconstruction.

Acknowledgments

This work was supported by NASA Contract NNA15BB15C to AMA, Inc. The authors would like to thank everyone on the MEDLI2 Reconstruction team for their insights and questions.

References

[1] Nelessen, A., Sackier, C., Clark, I., Brugarolas, P., Villar, G., Chen, A., Stehura, A., Otero, R., Stilley, E., Way, D., Edquist, K., Mohan, S., Giovingo, C., and Lefland, M., "Mars 2020 Entry, Descent, and Landing System Overview," *IEEE Aerospace Conference*, 2019.

[2] Gazarik, M., Wright, M., Little, A., Cheatwood, F., Herath, J., Munk, M., Novak, F., and Martinez, E., "Overview of the MEDLI Project," *IEEE Aerospace Conference*, 2008.

[3] Santos, J., Edquist, K., and Hwang, H., "White Paper for the Planetary Sciences Decadal Survey, 2023-2032: Entry, Descent, and Landing Instrumentation," Tech. rep., NASA, 2020.

[4] Wright, M., Beck, R., Edquist, K., Driver, D., Sepka, S., Slimko, E., and Willcockson, W., "Sizing and Margins Assessment of Mars Science Laboratory Aeroshell Thermal Protection System," *Journal of Spacecraft and Rockets*, Vol. 51, No. 4, 2014, pp. 1125–1138.

[5] Tran, H. K., Johnson, C. E., Rasky, D. J., Hui, F. C. L., Hsu, M.-T., and Chen, Y. K., "Phenolic Impregnated Carbon Ablators (PICA) for Discovery class missions," *AIAA Thermophysics Conference*, 1996.

[6] Willcockson, W. H., "Stardust Sample Return Capsule Design Experience," *Journal of Spacecraft and Rockets*, Vol. 36, No. 3, 1999, pp. 470–474.

[7] Beck, R., Driver, D., Wright, M., and Hwang, H., "Development of the Mars Science Laboratory Heatshield Thermal Protection System," *Journal of Spacecraft and Rockets*, Vol. 51, No. 4, 2014, pp. 1139–1150.

[8] Sepka, S., Wray, A., Prabhu, D., Kornieko, R., and Radbourne, C., "Testing of SLA-561V in NASA-Ames' Turbulent Flow Duct With Augmented Radiative Heating," *AIAA Thermophysics Conference*, 2011.

[9] Mahzari, M., Braun, R., White, T., and Bose, D., "Preliminary Analysis of the Mars Science Laboratory's Entry Aerothermodynamic Environment and Thermal Protection System Performance," *AIAA Aersopace Sciences Meeting*, 2013.

[10] Bose, D., White, T., Mahzari, M., and Edquist, K., "Reconstruction of Aerothermal Environment and Heat Shield Response of Mars Science Laboratory," *Journal of Spacecraft and Rockets*, Vol. 51, No. 4, 2014, pp. 1174–1184.

[11] White, T., Mahzari, M., Bose, D., and Santos, J., "Post-flight Analysis of Mars Science Laboratory's Entry Aerothermal Environment and Thermal Protection System Response," *AIAA Thermophysics Conference*, 2013.

[12] Mahzari, M., Braun, R., and Bose, D., "Inverse Estimation of the Mars Science Laboratory Entry Aeroheating and Heatshield Response," *Journal of Spacecraft and Rockets*, Vol. 52, No. 4, 2015, pp. 1203–1216.

[13] Tang, C., "MEDLI2: MISP Inferred Aerothermal Environment and Flow Transition Assessment," *AIAA SciTech Forum*, 2022. In press.

[14] Miller, R., "MEDLI2: MISP Measured Aftbody Aerothermal Environments," *AIAA SciTech Forum*, 2022. In press.

[15] Monk, J., Feldman, J., Mahzari, M., Santos, J., White, T., Prabhu, D., and Alpert, H., "MEDLI2 Material Response Model Development and Validation," *AIAA SciTech Forum*, 2022. In press.

[16] Schoenenberger, M., "Assessment of the Reconstructed Aerodynamics of the Mars 2020 Entry Vehicle," *AIAA SciTech Forum*, 2022. In press.

[17] Edquist, K., "Mars 2020 Reconstructed Aerothermal Environments and Design Margins," *AIAA SciTech Forum*, 2022. In press.

[18] Hwang, H., Bose, D., White, T., Wright, H., Schoenenberger, M., Kuhl, C., Trombetta, D., Santos, J., Oishi, T., Karlgaard, C., Mahzari, M., and Pennington, S., "Mars 2020 Entry, Descent, and Landing Instrumentation 2 (MEDLI2)," *AIAA Thermophysics Conference*, 2016.

[19] Karlgaard, C., "Mars Entry, Descent, and Landings Instrumentation 2 Trajectory and Atmosphere Reconstruction," *AIAA SciTech Forum*, 2022. In press.

[20] Chen, Y., and Milos, F., "Ablation and Thermal Response Program for Spacecraft Heatshield Analysis," *Journal of Spacecraft and Rockets*, Vol. 36, No. 3, 1999, pp. 475–483.

[21] Diaz, P., Meurisse, J., Brandis, A., Bessire, B., Barnhardt, M., and Yoon, S., "High-Fidelity Simulations of HyMETS Arc-Jet Flows for PICA-N Modeling," *AIAA SciTech Forum*, 2021.

[22] Chen, Y. K., "Thermal Analysis for Phenolic Impregnated Carbon Ablator/CV-1144-0 in Hypersonic Test Environments," *Journal of Spacecraft and Rockets*, 2021.

[23] Tiknonov, A., and Arsenin, V., *Solution of Ill-Posed Problems*, Winston and Sons, Washington, DC, 1977.

[24] Levenberg, K., "A Method for the Solution of Certain Non-linear Problems in Least Squares," *Quarterly of Applied Mathematics*, Vol. 2, No. 2, 1944, pp. 164–168.

[25] Marquardt, D., "An Algorithm for Least-Squares Estimation of Nonlinear Parameters," *Journal of the Society for Industrial and Applied Mathematics*, Vol. 11, No. 2, 1963, pp. 431–441.